International Journal of Machine Tools & Manufacture 68 (2013) 81–90

Contents lists available at SciVerse ScienceDirect

International Journal of Machine Tools & Manufacture

journal homepage: www.elsevier.com/locate/ijmactool

Rapid evaluation and optimization of machine tools with position-dependent stability

Mohit Law, Yusuf Altintas *, A. Srikantha Phani

Department of Mechanical Engineering, The University of British Columbia, 2054-6250 Applied Science Lane, Vancouver, BC, Canada, V6T 1Z4

ARTICLE INFO

Article history:
Received 14 November 2012
Received in revised form
4 February 2013
Accepted 6 February 2013
Available online 21 February 2013

Keywords:
Machine tool
Model reduction
Stability
Optimization

ABSTRACT

Machine tool's productivity is a function of the dynamic response between the spindle nose and table, which varies as a function of drive positions within the machine work volume. The position-dependent structural dynamics results in varying stability of the machine. This paper presents a computationally efficient methodology to evaluate and improve dynamic performance of a machine tool at the design stage. An efficient position-dependent multibody dynamic model of a machine tool is developed based on reduced model substructural synthesis. The experimentally validated reduced machine model simulates position-dependent behavior with significantly less computational effort than commonly used full order Finite Element models. The proposed modeling strategy is used to identify weak components of an experimental machine, which limit the productivity due to chatter. The identified weak machine component is modified and the complete dynamics are rapidly analyzed by virtually re-assembling the machine using reduced order models. Optimal design modifications are shown to increase productivity by ~25%. The proposed method can be used for efficient simulation of structural dynamics, stability assessment as well as interactions of the CNC and cutting process with the machine tool structure in a virtual environment.

1. Introduction

The present machine tool industry requires rapid analysis of structural dynamics, machine-cutting process and controller interactions in a virtual environment. The process–machine interactions are influenced by the dynamic stiffness between the tool center point (TCP) and workpiece which determines the maximum depth of cut due to chatter constraints. The dynamic stiffness and the maximum stable depth of cut are further influenced by the changing structural dynamics of the machine as the tool moves along the tool path in the machine work volume. The position-varying structural vibrations between the TCP and servo drives further limit the positioning speed and accuracy. The objective of the machine tool designer is to maximize the dynamic stiffness between TCP—workpiece and TCP—drive motors while keeping the machine mass light for high speed positioning and high-productivity machining. Evaluation and optimization of machine tool's performance to deliver improved dynamic behavior over the whole work volume necessitates rapid assessment of several design alternatives in the virtual environment before eventual physical prototyping [1].

Typically, machine tool design and response analyses are carried out in virtual environments using a finite element (FE) model of the machine. These models are efficient for subsystem level design analyses such as modeling of ball-screw feed-drive systems [2], and spindles [3,4]. FE models for full machine analyses have also proven to be useful for structural modification based on process–machine interactions [5–7], as well as for modeling control structure interactions [8]. However, response analyses of full machine models which are typically on the order of 1,000,000 degrees of freedom (DOFs) or more, is computationally costly, and can take up significant portion of the total computational effort required for the design and analyses of machine tools [9]. Moreover, modeling position-dependency in such large order FE models requires cumbersome adaptive/ re-meshing strategies, making it time consuming in practice.

Position-dependency has been modeled using co-simulation techniques in which FE solvers are coupled to multibody simulation codes [10–12]. These methods have been shown to be effective for rigid-flexible body motion analyses and are less suited to the flexible bodies of a machine undergoing relative motion. Changing structural dynamics have also been modeled with simplifying assumptions of modeling the multiple flexible bodies in contact as rigid-flexible [13,14]. Position-dependency for multiple flexible bodies in contact was also modeled in [15] for a simplified single set nodal compatibility condition. Increasing modularity in the machine tool development process often requires substructures to be designed and modeled separately, resulting in different mesh resolutions at the contacting interface.

* Corresponding author. Tel.: +1 604 822 5622; fax: +1 604 822 2403.
E-mail addresses: altintas@mech.ubc.ca, altintas@mail.ubc.ca (Y. Altintas).

0890-6955/$ - see front matter © 2013 Elsevier Ltd. All rights reserved.
http://dx.doi.org/10.1016/j.ijmachtools.2013.02.003

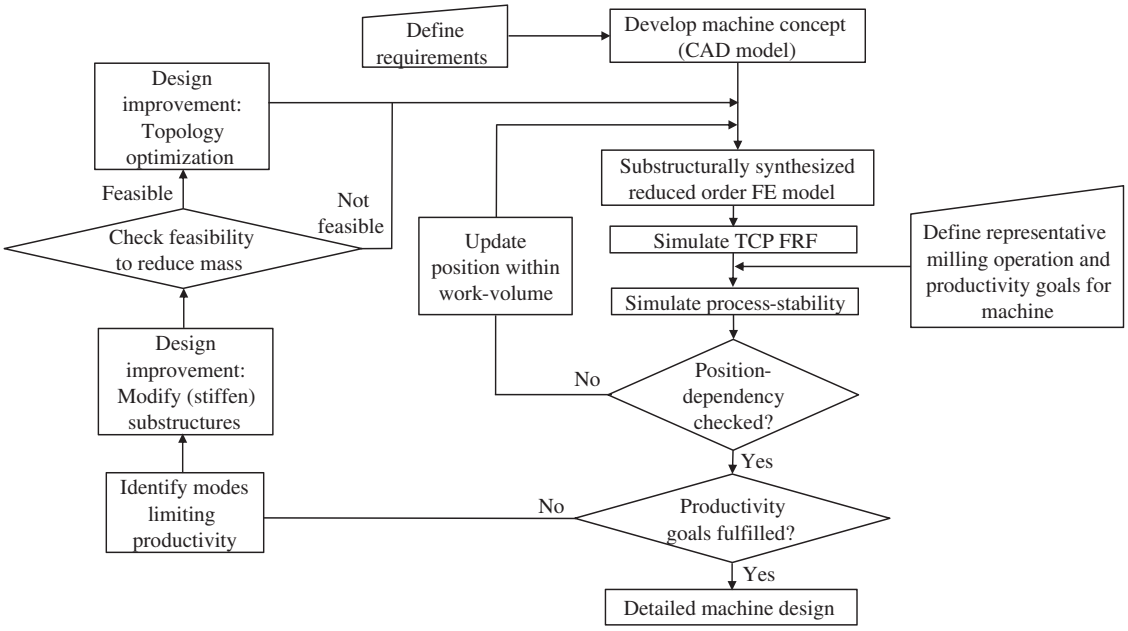

Fig. 1. Flow chart of a virtual integrated position-dependent process–machine interaction approach for designing milling machines ensuring targeted productivity.

Ensuring mesh compatibility during synthesis for such models which are simultaneously in contact over multiple nodes is difficult to guarantee, and if this condition was not necessary—modeling time could be halved, as estimated in [9].

To facilitate rapid assessment of design alternatives, this paper offers an integrated virtual approach based on a computationally efficient position-dependent multibody dynamic model of the machine. A reduced model substructural synthesis approach proposed earlier by the authors in [16] is extended here to model the entire machine tool system. Position-dependency is modeled by synthesizing reduced substructures whose response is position-independent. This approach allows for modularity in the design process by tolerating mesh incompatibility at substructural interfaces by having displacement compatibility between adjacent substructures through sets of algebraic constraint equations.

Position-dependent dynamic behavior of a representative three-axis vertical machining center—FADAL 2216 is modeled and assessed using the generalized integrated virtual design scheme shown in Fig. 1. Position and feed-direction-dependent-process-stability is proposed as a performance criterion to evaluate the productivity of the machine tool in its entire work volume. This criterion also identifies parameters limiting the target productivity levels. Improvements to meet design targets, if necessary, are made possible with the iterative approach as shown in Fig. 1.

The paper is organized as follows: a generalized substructural synthesis formulation to model position-dependency is presented in Section 2. The virtual machine model is compared with experimental results in Section 3. For a defined set of cutting conditions and productivity levels, the position and feed-direction-dependent stability is evaluated in Section 4. Mechanical parameters limiting productivity are identified and modified to meet target productivity in Section 5; followed by conclusions in Section 6.

2. Generalized substructural formulation for position-dependency

Position-dependency at the TCP is modeled based on a two stage substructural assembly approach. At first, each of the major substructures of the machine under consideration, namely: spindle–spindle-housing, column, base, cross-slide, and table are reduced independently and synthesized subsequently together with the three individual feed drive models as shown in Fig. 2. A second stage substructural assembly involves coupling the tool–tool-holder response (Substructure I) to the response obtained at the spindle nose from the first stage (Substructure II) using a receptance coupling approach. This allows different tool–tool-holder combinations to be modeled independently and coupled subsequently without having to regenerate machine (spindle) models [17].

FE models for the structural substructures are generated from their respective CAD models using 10 noded solid tetrahedron elements with material properties assigned as: modulus of elasticity of 89 GPa; density of 7250 kg/m^3; and, Poisson's ratio of 0.25. The spindle, three ball-screw drive models and the tool–tool-holder are modeled with Timoshenko beam elements. The spindle assembly including the spindle shaft, cartridge, bearings, drive pulley, and other accessories such as nuts and rotary couplings are modeled based on work reported by Cao and Altintas [3]. This spindle assembly is integrated as a separate substructure coupled rigidly to the spindle housing. Each of the substructural models is exported, after convergence checks, to the MATLAB environment for reduction and synthesis.

2.1. Substructure model reduction

Each of the main substructural machine components is reduced independently as discussed here. For any substructure under consideration, the undamped equations of motion are represented as:

$$\boldsymbol{M}\ddot{\boldsymbol{u}}+\boldsymbol{K}\boldsymbol{u}=\boldsymbol{f} \tag{1}$$

where $\{\boldsymbol{M},\boldsymbol{K}\}_{F\times F}$ are the mass and stiffness matrices for the total DOFs F; and $f_{F\times 1}$ is the force vector. Reduced substructures are synthesized at their interface DOFs. Hence the displacement vector $\boldsymbol{u}$ is partitioned into the DOFs to be retained, i.e. the exterior/interface (E) DOFs, $\boldsymbol{u}_E$, that are in physical contact with the other substructure(s), and, the DOFs which are to be eliminated, i.e. the interior (I) DOFs, $\boldsymbol{u}_I$.

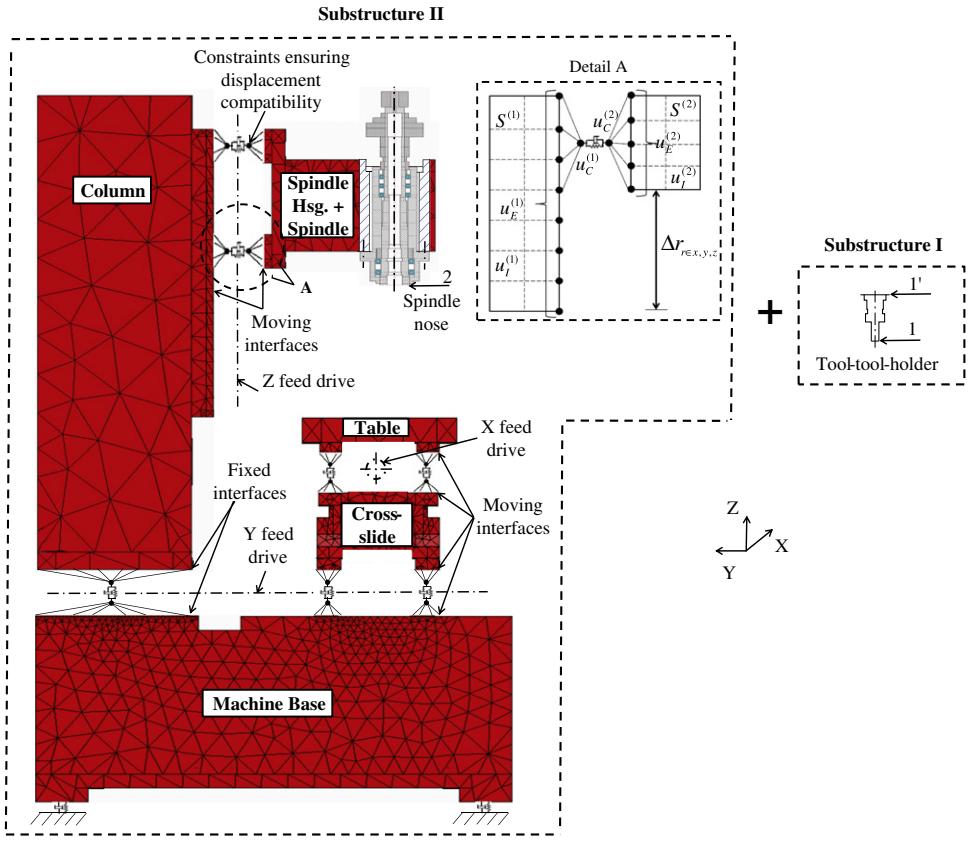

Fig. 2. Two stage substructural synthesis of the machine tool. Tool–tool-holder response (Substructure I) is coupled to the position-dependent response of the synthesized substructural machine model (Substructure II).

Table 1
Division of DOFs for individual substructures.

		Spindle–spindle housing	Column	Base	Cross-slide	Table	Total
Reduced model	Full order model	21,992	45,983	97,214	50,201	15,623	231,013
	Interface DOFs (u_E)	1037	1533	1945	2598	1908	
	Significant component modes (P)	27	28	46	27	24	9173

The displacement vector $\boldsymbol{u}$ is expressed in terms of a reduced set $\mathbf{u}_{R_{R\times 1}}$ by a transformation matrix $\boldsymbol{T}_{F\times R}(R \ll F)$ as:

$$\boldsymbol{u}_{F\times 1} = \boldsymbol{T}_{F\times R}\boldsymbol{u}_{R_{R\times 1}} \tag{2}$$

where

$$\boldsymbol{T} = \begin{bmatrix} \boldsymbol{I}_{EE} & \boldsymbol{0}_{EP} \\ \boldsymbol{T}_{ICMS_{IE}} & \boldsymbol{\Phi}_{IP} \end{bmatrix} \tag{3}$$

is a modified form of the standard component mode synthesis (CMS) transformation matrix as previously presented by the authors in [16]. $\boldsymbol{I}_{EE}$ is a unit matrix, and, $\boldsymbol{T}_{ICMS}$ is an improvement over the equivalent quasi-static transformation obtained by including the inertial terms [16].

The effect of the interior DOFs is modeled by complementing the reduced set of exterior DOFs by a set of generalized (modal) coordinates represented by selecting modes belonging to the interior DOFs. This is done by selecting a subset of significant P modes, i.e. $\boldsymbol{\Phi}_{IP} \subseteq \boldsymbol{\Phi}_{II}$ in Eq. (3); wherein the eigenvector $\boldsymbol{\Phi}_{II}$ is obtained by solving the eigenvalue problem corresponding to the interior DOFs. The selected mode sets are able to represent higher order dynamics of the substructure while keeping the order of the reduced model to a minimum by spanning a much wider frequency range with fewer modes than would be required with standard CMS methods. For further details on reduction procedure and significant mode selection criteria, see [16].

Using the transformation matrix of Eq. (3), the reduced substructural matrices $\{\boldsymbol{M}_R,\boldsymbol{K}_R\}_{R\times R}$ are represented as:

$$\boldsymbol{M}_R = \boldsymbol{T}^{\mathrm{T}}\boldsymbol{M}\boldsymbol{T}; \quad \boldsymbol{K}_R = \boldsymbol{T}^{\mathrm{T}}\boldsymbol{K}\boldsymbol{T}; \quad \boldsymbol{f}_R = \boldsymbol{T}^{\mathrm{T}}\boldsymbol{f}. \tag{4}$$

The size of each of the reduced models which consists of the exterior/interface DOFs $\boldsymbol{u}_E$, complemented by a set of P significant modes is listed in Table 1.

2.2. Substructural synthesis

Each of the reduced substructures are synthesized at the contacting interfaces as shown in detail "A" in Fig. 2, where the substructures $S^{(1)}$ and $S^{(2)}$ may represent any of the machine tool substructural components with/without relative motion between them. Each substructure has been modeled separately resulting in different mesh resolutions at their contacting interfaces. To synthesize such incompatible substructures, an approximate model of surface interaction is obtained by defining a virtual condensation node placed at the center of each of the interface surfaces in contact, as shown in the detail "A" in Fig. 2.

Displacement compatibility between the virtual nodes for substructures in rigid contact is represented as [16]:

$$\boldsymbol{u}_C^{(1)} - \boldsymbol{u}_C^{(2)} = 0 \tag{5}$$

The displacement of the virtual node $\boldsymbol{u}_C^{(n)}$ for substructure $n(n=1,2)$ consisting of a set of translational and rotational DOFs $(\boldsymbol{u}_C \supset x_C, y_C, z_C, \theta_{x_C}, \theta_{y_C}, \theta_{z_C})$ is linked to the interface DOFs with a displacement operator such that:

$$\boldsymbol{u}_C^{(n)} = \boldsymbol{C}^{(n)} \boldsymbol{u}^{(n)} \tag{6}$$

Coefficients of the displacement operator $\boldsymbol{C}^{(n)}$ are extracted by linking the DOFs of the condensation node to the interface nodal DOFs it is meant to represent using a multipoint constraint (MPC) equation formulation. The MPCs represent the DOFs of the condensation node as a linear combination of all the DOFs of the nodes in contact at the interface.

The motion of the condensation node, i.e. displacements ($\boldsymbol{u}_C$) and rotations ($\boldsymbol{\alpha}_C$) are fully described as the weighted average of the motion of the interface nodes in contact as [18]:

$$\begin{aligned} \boldsymbol{u}_C &= \frac{\sum_{k=1}^{m} w_{\mathrm{E}_k} \boldsymbol{u}_{\mathrm{E}_k}}{\sum_{k=1}^{m} w_{\mathrm{E}_k}} \\ \boldsymbol{\alpha}_C &= \frac{\sum_{k=1}^{m} w_{\mathrm{E}_k} \boldsymbol{r}_{C_k} \times \boldsymbol{u}_{\mathrm{E}_k}}{\sum_{k=1}^{m} w_{\mathrm{E}_k} |\boldsymbol{r}_{C_k}|^2} \end{aligned} \tag{7}$$

where w_{E_k} represents the weight factors for each of the exterior DOFs corresponding to the node k in contact at a particular position. $\boldsymbol{r}_{C_k}$ is the vector from the condensation node to the node corresponding to the interface node k. Eq. (7) results in a set of m constraint equations. The set of nodal DOFs for each node k for volumetric elements in this work is: $\boldsymbol{u} \supset x_k, y_k, z_k$. To ensure that the condensation node represents the average motion of the contacting interface surface it is meant to represent, the weight factors w_{E_k} for each DOF are chosen proportional to the part of the interface surface its node represents; and are assigned as the coordinates of the nodes being coupled in this study. For additional details on selection of weight factors, see [16].

Synthesizing each substructural interface with a set of m constraint equations, the undamped equation of motion for the synthesized reduced model at a particular position is:

$$\begin{bmatrix} \boldsymbol{M}_{R_S} & 0 & 0 & 0 & 0 & 0 \\ 0 & \boldsymbol{M}_{R_C} & 0 & 0 & 0 & 0 \\ 0 & 0 & \boldsymbol{M}_{R_B} & 0 & 0 & 0 \\ 0 & 0 & 0 & \boldsymbol{M}_{R_{CS}} & 0 & 0 \\ 0 & 0 & 0 & 0 & \boldsymbol{M}_{R_T} & 0 \\ 0 & 0 & 0 & 0 & 0 & 0 \end{bmatrix} \begin{Bmatrix} \ddot{\boldsymbol{u}}_{R_S} \\ \ddot{\boldsymbol{u}}_{R_C} \\ \ddot{\boldsymbol{u}}_{R_B} \\ \ddot{\boldsymbol{u}}_{R_{CS}} \\ \ddot{\boldsymbol{u}}_{R_T} \\ \ddot{\boldsymbol{\lambda}} \end{Bmatrix}$$
$$+ \begin{bmatrix} \boldsymbol{K}_{R_S} & 0 & 0 & 0 & 0 & \boldsymbol{C}^T \\ 0 & \boldsymbol{K}_{R_C} & 0 & 0 & 0 & \boldsymbol{C}^T \\ 0 & 0 & \boldsymbol{K}_{R_B} & 0 & 0 & \boldsymbol{C}^T \\ 0 & 0 & 0 & \boldsymbol{K}_{R_{CS}} & 0 & \boldsymbol{C}^T \\ 0 & 0 & 0 & 0 & \boldsymbol{K}_{R_T} & \boldsymbol{C}^T \\ \boldsymbol{C} & \boldsymbol{C} & \boldsymbol{C} & \boldsymbol{C} & \boldsymbol{C} & 0 \end{bmatrix} \begin{Bmatrix} \boldsymbol{u}_{R_S} \\ \boldsymbol{u}_{R_C} \\ \boldsymbol{u}_{R_B} \\ \boldsymbol{u}_{R_{CS}} \\ \boldsymbol{u}_{R_T} \\ \boldsymbol{\lambda} \end{Bmatrix} = \begin{Bmatrix} \boldsymbol{f}_{R_S} \\ \boldsymbol{f}_{R_C} \\ \boldsymbol{f}_{R_B} \\ \boldsymbol{f}_{R_{CS}} \\ \boldsymbol{f}_{R_T} \\ 0 \end{Bmatrix} \tag{8}$$

where $\{\boldsymbol{M}_R, \boldsymbol{K}_R\}$ are the reduced substructural mass and stiffness matrices and the subscripts S, C, B, CS, and T correspond to the spindle–spindle housing combine, column, base, cross-slide, and table respectively. $\boldsymbol{C}(\boldsymbol{u}_{R_S}, \boldsymbol{u}_{R_C}, \boldsymbol{u}_{R_B}, \boldsymbol{u}_{R_{CS}}, \boldsymbol{u}_{R_T})$ is the displacement operator coupling these substructures, whose coefficients are obtained from Eqs. (5)–(7). $\boldsymbol{\lambda}$ represents a discrete set of m Lagrange multipliers corresponding to the number of constraint equations [19].

The synthesized model enables prediction of dynamic response at the spindle nose as one component changes its position relative to another by solving the eigenvalue problem form of Eq. (8), by varying the tool position in the work volume by adjusting ΔX, ΔY, or ΔZ (see Fig. 2). For each new position, since a new set of nodes come into contact, while others fall out of contact, the displacement operator in Eq. (6) is updated by instantaneously coupling/decoupling the corresponding nodes on the interfaces.

Since the substructurally synthesized reduced machine model size is ~1/25th the size of the full model (Table 1), it allows for very efficient position-dependent dynamic modeling of the machine. Further modularity in the design process is facilitated by synthesizing the frequency response function (FRF) at the spindle nose with that of separately modeled tool–tool-holder model response as discussed in the next section.

2.2.1. Tool point FRF with receptance coupling

Since both the spindle and the tool–tool-holder are modeled with Timoshenko beam elements, each of the coupling nodes has six DOFs, three translational and three rotational; for which the respective component receptances in compact matrix form are:

$$\begin{Bmatrix} u_x \\ u_y \\ u_z \\ \theta_x \\ \theta_y \\ \theta_z \end{Bmatrix}_i = \begin{bmatrix} h_{xx} & h_{xy} & h_{xz} & l_{xm_x} & l_{xm_y} & l_{xm_z} \\ h_{yx} & h_{yy} & h_{yz} & l_{ym_x} & l_{ym_y} & l_{ym_z} \\ h_{zx} & h_{zy} & h_{zz} & l_{zm_x} & l_{zm_y} & l_{zm_z} \\ t_{\theta_x f_x} & t_{\theta_x f_y} & t_{\theta_x f_z} & p_{\theta_x m_x} & p_{\theta_x m_y} & p_{\theta_x m_z} \\ t_{\theta_y f_x} & t_{\theta_y f_y} & t_{\theta_y f_z} & p_{\theta_y m_x} & p_{\theta_y m_y} & p_{\theta_y m_z} \\ t_{\theta_z f_x} & t_{\theta_z f_y} & t_{\theta_z f_z} & p_{\theta_z m_x} & p_{\theta_z m_y} & p_{\theta_z m_z} \end{bmatrix}_{ij} \begin{Bmatrix} f_x \\ f_y \\ f_z \\ m_x \\ m_y \\ m_z \end{Bmatrix}_j \tag{9}$$

where h represents the displacement-to-force receptance; l represents the displacement-to-couple receptance; t represents the rotations-to-force receptance; and p represents the rotation-to-couple receptance; and i and j are the respective measurement and excitation locations. Eq. (9) may be rewritten in its generalized form as:

$$\boldsymbol{x}_i = \boldsymbol{R}_{ij} \boldsymbol{q}_j \tag{10}$$

where $\boldsymbol{R}_{ij}$ is the generalized receptance matrix that describes both translational and rotational component behavior, and, $\boldsymbol{x}_i$ and $\boldsymbol{q}_j$ are the corresponding generalized displacement/rotation and force/couple vectors.

The direct receptances at, and cross receptances between the free-end (i.e. location 1 in Fig. 2) and the coupling end (location 1′ in Fig. 2) of the tool–tool-holder model are:

$$\boldsymbol{x}_1 = \boldsymbol{R}_{11} \boldsymbol{q}_1 \tag{11}$$

$$\boldsymbol{x}_{1'} = \boldsymbol{R}_{1'1'} \boldsymbol{q}_{1'} \tag{12}$$

$$\boldsymbol{x}_1 = \boldsymbol{R}_{11'} \boldsymbol{q}_{1'} \tag{13}$$

Due to symmetry and Maxwell's reciprocity, $\boldsymbol{R}_{11'} = \boldsymbol{R}_{1'1}$. The direct receptances at the spindle nose (location 2 in Fig. 2) are similarly represented as:

$$\boldsymbol{x}_2 = \boldsymbol{R}_{22} \boldsymbol{q}_2 \tag{14}$$

Ensuring displacement compatibility, i.e. $\boldsymbol{x}_{1'} - \boldsymbol{x}_2 = 0$, and force equilibrium, i.e. $\boldsymbol{q}_{1'} + \boldsymbol{q}_2 = 0$, at the rigid connection between the tool–tool-holder and the spindle nose, the assembled receptances, G_{11}, at the TCP in the generalized form are given as [20]:

$$\boldsymbol{G}_{11} = \boldsymbol{R}_{11} - \boldsymbol{R}_{11'} (\boldsymbol{R}_{1'1'} + \boldsymbol{R}_{22})^{-1} \boldsymbol{R}_{1'1} \tag{15}$$

where $\boldsymbol{G}_{11}$ has the same structure as $\boldsymbol{R}_{ij}$, and its constituent receptances are obtained from solutions in Eqs. (11)–(14).

The two stage substructural synthesis methodology yields the position-dependent dynamic response at the TCP. A face-mill cutter of 50 mm diameter with an overhang of 70 mm from the spindle nose with a CAT40 type tool-holder is modeled and its response is obtained from Eqs. (11)–(13). Response at the spindle nose obtained from Eqs. (8) and (14) is synthesized with the tool–tool-holder response, which leads to the response at the free-end of the tool using Eq. (15).

2.3. Position-dependent dynamic response at TCP for machine model

TCP FRFs are simulated with the substructurally synthesized reduced order machine model at three different positions of the machine. The top position is the configuration shown in Fig. 2; the mid and bottom positions are when the tool has moved in the Z-direction by an amount of -0.2 m; and -0.4 m respectively. A uniform damping ratio of $\zeta=0.02$ has been assumed in simulating FRFs, which is updated by correlating with experimental modal damping from measurements on a similar available machine as presented in the following section. The stability of the machining process is primarily influenced by the low-frequency structural modes [6] such as column, table, spindle housing, and the spindle shaft; hence X and Y directional direct TCP FRFs are compared up until 350 Hz in Fig. 3. Higher frequency tool and tool-holder modes are usually not related to the design of the machine tool structure since they are machining application specific and are more local in nature, i.e. they do not exhibit strong position-dependency.

As evident in Fig. 3, the global modes corresponding to the column (30–100 Hz) exhibit stronger position-dependency as compared to the spindle housing modes (100–350 Hz). The low-frequency column mode in the X direction at $\sim$40 Hz varies by $\sim$50% in dynamic stiffness, whereas the second X directional column bending mode at $\sim$70 Hz varies by up to 8% in natural frequencies. The dominant low-frequency column mode in the Y direction at $\sim$45 Hz varies by as much as 15% in natural frequencies and $\sim$135% in dynamic stiffness over the full Z stroke of the machine.

Dominant low-frequency mode shapes for the reduced model when the headstock is at the top position are shown in Fig. 4. The full model shown in Fig. 4(a) is represented by only the interface DOFs in Fig. 4(b). Mode shapes are shown by overlaying the deformed configuration over the un-deformed configuration. The first mode at $\sim$41 Hz corresponds to a global column bending mode in the YZ plane, in Fig. 4(c), while the second dominant mode at $\sim$42 Hz corresponds to the global column bending mode in the XZ plane, in Fig. 4(d).

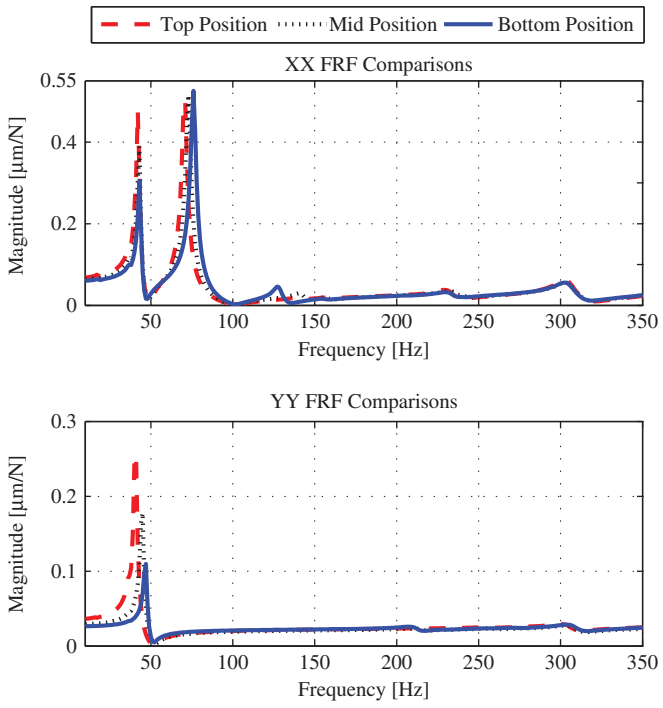

Fig. 3. Comparison of reduced model TCP FRFs at three different tool positions: top, mid, and bottom.

Position-dependent results for the dominant low frequency modes obtained with the reduced model are compared with the full order model results in Table 2, which also includes error estimates rounded off to the nearest integer. Full order results are obtained by 'gluing' substructures at the interfaces in the ANSYS® environment [21]. As the comparison shows, the synthesized reduced model is able to reasonably capture full order model behavior with errors in natural frequencies ranging from 2% to 10% for the dominant X directional modes; and by at most 18% for the dominant Y directional mode. Dynamic stiffness too is approximated reasonably well with errors ranging from 0% to 9%; with the exception of the X-directional mode at $\sim$42 Hz, for which error in approximation is as much as $\sim$50%. Errors are mainly thought to be due to the interpolation constraint formulation underestimating contact stiffness at the interfaces [18], leading to underestimation of stiffness of overall assembled machine. Other sources of errors may be attributed to modeling simplifications, and to a lesser extent due to the reduction process [16]. Overall however, even though the synthesized reduced model is $\sim$1/25th the size of the full model, yet it gives reasonably close results; and importantly, the reduced model leads to considerable simulation time savings for the designer; taking $\sim$1 min/position as compared to $\sim$12 h/position for the full model (Intel® i7 2.67 GHz processor with 9 GB RAM) thereby facilitating position-dependent analyses. The verified reduced model is validated against measurements by considering joint characteristics in the next section.

3. Validation of the substructurally synthesized reduced machine model

Dynamic response is measured at the tool tip with a 50 mm diameter face mill on the three axis machine—FADAL2216, shown in Fig. 5. Measurement including data acquisition, modal analysis and FRF curve fitting is carried out with CUTPRO® [22]. Measured modal damping ratio is used in the synthesized reduced machine model and the full machine model. Joints at the contacting interfaces are idealized as two translational springs perpendicular to the direction of motion. The connections between the tool–tool holder-spindle and between the spindle–spindle housing are assumed to be rigid. The joint stiffness at bolted interfaces are taken as the corresponding bolt's stiffness. Detailed modeling of the contact stiffness at the rolling interfaces is beyond the present scope of this paper; in which interfaces are idealized as being connected by linear spring elements for which the equivalent contact stiffness values were obtained from manufacturers' catalogs [23]. Equivalent contact stiffness for each of the three axes for the guide-block and guide-rail interface is assigned as 187 N/μm (THK SVR series); and as 280 N/μm for the ball-screw–nut interface (THK SBN series) [23].

Although the joint characteristics are a function of contacting surface conditions which vary over the entire contacting interface, for simplicity, joint parameters are assumed to be position-independent. Measured fitted FRFs and simulated (full, reduced) TCP FRFs are compared in Fig. 6 in both the X and Y machine directions for the representative position of the tool being at the bottom of the work volume.

Though the model predicted response is able to capture the trend of the measured response as evident in Fig. 6; the dynamic stiffness of the low-frequency column modes is underestimated, particularly in the X-direction. The model predicted response also overestimates the first bending mode in the YZ plane—predicted at 47 Hz, and measured at 33 Hz. These anomalies are mainly

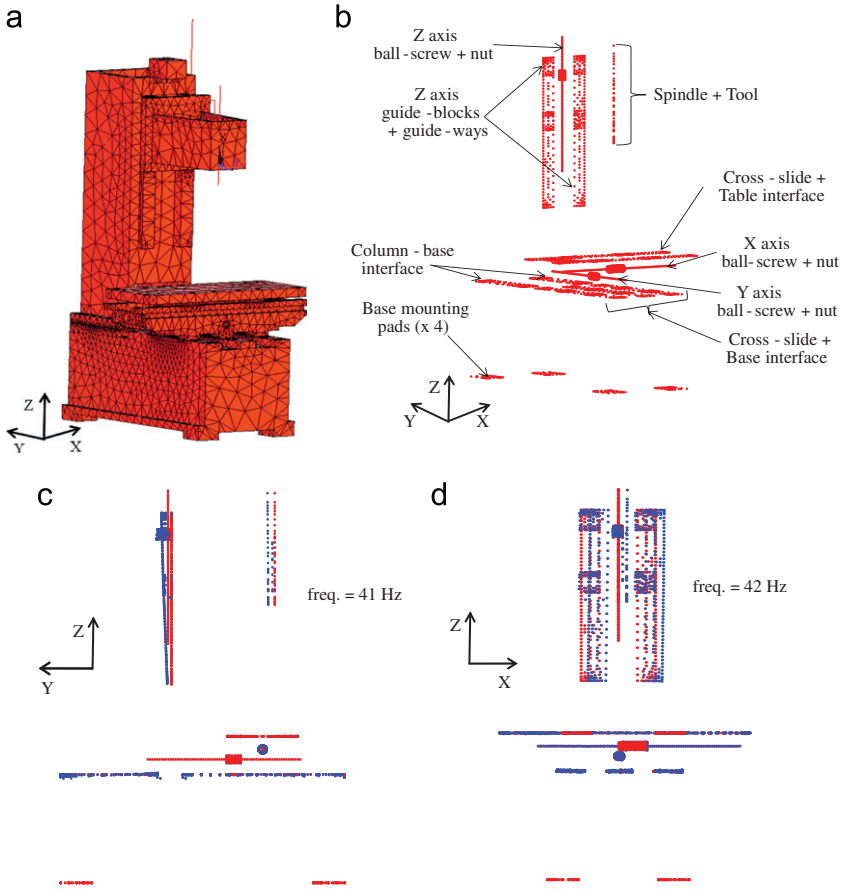

Fig. 4. (a) Full order model, (b) reduced model with only interface DOFs, (c) mode shape of column bending mode in YZ plane, and (d) mode shape of column bending mode in XZ plane.

Table 2
Comparison of dominant modes for full order model (***F***) and reduced order model (***R***), and the error estimates (***E***) in the *X* and *Y* directions. Natural frequencies (f_n) [Hz]; dynamic stiffness (K_d) [N/μm]; error [%].

		Bottom position						**Mid position**						**Top position**					
		f_n			K_d			f_n			K_d			f_n			K_d		
	Mode no.	***F***	***R***	% **E**	***F***	***R***	% **E**	***F***	***R***	% **E**	***F***	***R***	% **E**	***F***	***R***	% **E**	***F***	***R***	% **E**
***X* direction**	1	42	43	2	6.7	3.2	−52	41	43	5	3.5	2.6	−26	40	42	5	3.6	2.1	−42
	2	81	76	−6	1.8	1.9	6	80	73	−9	1.9	1.9	–	79	71	−10	1.9	2	5
***Y* direction**	1	56	47	−16	9.9	9.2	−7	52	45	−13	5.9	5.7	−3	50	41	−18	4.3	3.9	−9

thought to be due to the difficulty in modeling the base-mounting springs whose contact stiffness if overestimated, leads to errors in prediction of the low-frequency modes. Order mismatch between the number of simulated and measured modes between 50 and 100 Hz and at ~250 Hz may be attributed to modeling simplifications in representing the machine accessories like the automatic tool changer and cabinets by lumped mass elements.

The model response is updated at other positions as well, and is used to evaluate the achievable productivity levels of the machine tool in the next section.

4. Material removal rate and position-dependent stability

When the structural dynamics of the machine vary within the machine's work space, the chatter stability and the resulting limits on the material removal rates vary as well. The variation of stability is demonstrated here by considering face milling of AISI 4340 steel with 80% engagement, which is treated as the target application for the envisaged machine. A minimum speed and feed-direction independent stable depth of cut of 4 mm is targeted in the whole working range of the machine. Effects of position-dependent directional compliances on machining stability are investigated by generating feed-direction-dependent absolute machining stability charts.

4.1. Oriented FRFs and feed-direction-dependent stability

A multi-degree-of-freedom machine tool may chatter in any of its dominant modes. The effect of each mode is determined by its dynamic characteristics; whether or not the mode is aligned with the principal machine directions ($X_{MT}Y_{MT}$); and, the direction of feed. Consider a machine tool with horizontal (x) and normal (y) axes; and let the tool be traveling in the feed direction (u) with an angular orientation (θ) as shown in Fig. 7. Additionally, if the structural mode ($\overline{m}_i^{xy}$) is not aligned with the principal machine

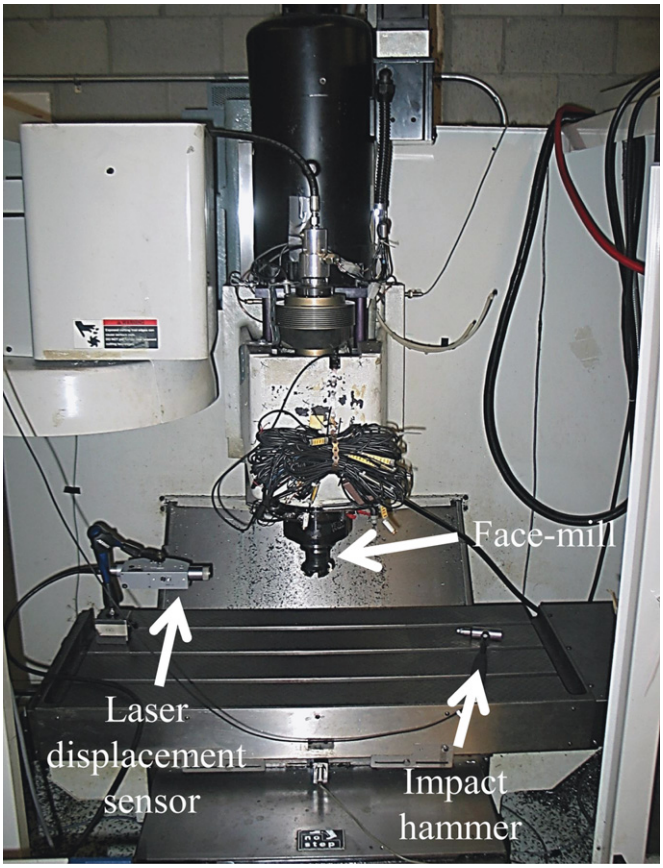

Fig. 5. Experimental setup to measure TCP FRFs on machine.

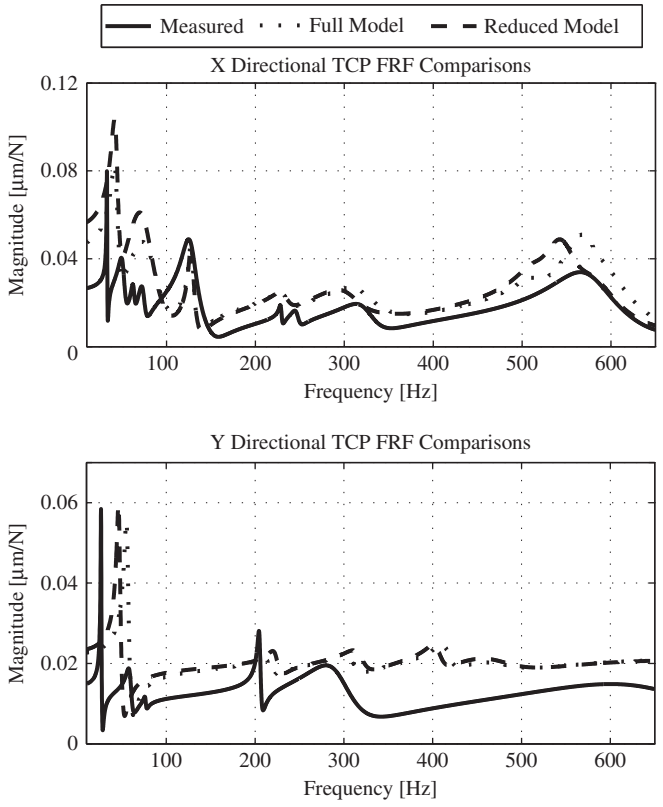

Fig. 6. TCP FRF comparisons between measured and updated full model and substructurally synthesized reduced model.

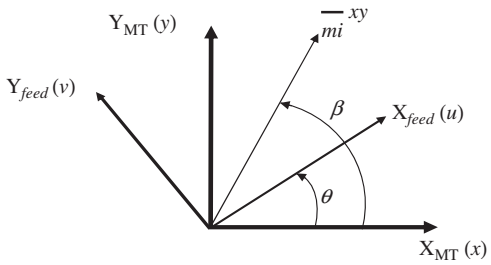

Fig. 7. Orientation of machine mode $\overline{m}_i^{xy}$ in the machine tool axes ($X_{MT}Y_{MT}$) and the feed axes ($X_{feed}Y_{feed}$).

tool directions, it would be oriented with an angular distance (β) as also shown in Fig. 7.

The stability of the milling system is determined using a modal model of the machine and the following characteristic equation [24]:

$$det([\boldsymbol{I}]+\Lambda[\boldsymbol{\Phi}_{OR}(i\omega_c)])=0 \tag{16}$$

The complex eigenvalue (Λ) in Eq. (16) is defined as:

$$\Lambda=\Lambda_R+i\Lambda_I=-\frac{1}{4\pi}N_tK_ta(1-e^{-i\omega_cT}) \tag{17}$$

where Λ_R and Λ_I are its real and imaginary parts; N_t is the number of teeth on the cutter; K_t is the tangential cutting force coefficient of the work-material; a is the axial depth of cut; ω_c is the chatter frequency; and, T is the tooth passing period.

The oriented directional matrix, $\boldsymbol{\Phi}_{OR}$, within Eq. (16) is expressed as:

$$[\boldsymbol{\Phi}_{OR}]=[\boldsymbol{\alpha}_0][\boldsymbol{\Phi}_{uv}] \tag{18}$$

where α_0 is the matrix of the average direction factors determined as presented by Altintas and Budak in [24]. The transfer function matrix, $\boldsymbol{\Phi}_{uv}$, at the TCP in the feed plane is expressed as [25]:

$$[\boldsymbol{\Phi}_{uv}]=[\boldsymbol{R}][\boldsymbol{\Phi}_{xy}][\boldsymbol{R}]^{-1} \tag{19}$$

where $\boldsymbol{R}(\beta,\theta)$ is a rotational matrix used to project the vibrations in the machine tool principal directions, i.e. $\boldsymbol{\Phi}_{xy}$ into the feed (uv) directions. Assuming the principal modes to be aligned with the machine tool axes, i.e. with $\beta=0$; the rotational matrix within Eq. (19) becomes:

$$\boldsymbol{R}=\begin{bmatrix}\cos\theta & -\sin\theta\\ \sin\theta & \cos\theta\end{bmatrix} \tag{20}$$

The absolute speed independent limiting depth of cut, described by the parameters in Eqs. (16) and (18), for different feed directions (0–360°) is analytically determined as given in [24]:

$$a_{lim_{feed}}=-\frac{2\pi\Lambda_R}{N_tK_t}\left[1+\left(\frac{\Lambda_I}{\Lambda_R}\right)^2\right]. \tag{21}$$

Solution to Eq. (21) for each tool position within the work volume results in speed independent absolute minimum stable depths of cut which vary across feed directions in proportion to the magnitude of projections of the modes in that direction.

4.2. Process-stability and modes limiting productivity

Feed-directional stability was simulated for face milling AISI 4340 steel with $N_t=5$; $K_t=3000$ MPa; and the radial coefficient, $K_r=0.24$. Results for three tool positions along with the corresponding chatter frequencies are shown in Fig. 8. The structural modes that are less than 650 Hz, and, that are position-dependent, are considered since they reflect the design characteristics

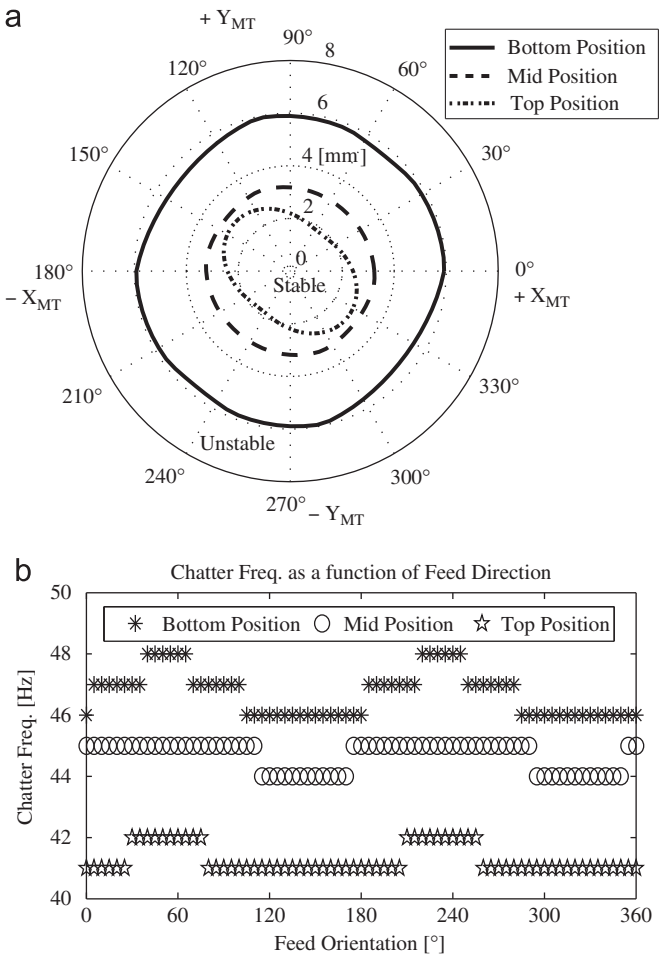

Fig. 8. (a) Feed directional stability at three different tool positions: top, mid, and bottom, and (b) corresponding chatter frequencies as a function of feed direction.

of the machine tool. In Fig. 8(a), the regions inside the stability curve envelopes are stable, and those outside the process stability threshold, are unstable. The absolute limiting depth of cut is plotted radially, while the machining (feed) directions are plotted circumferentially. The stability curves are symmetric about 45° and 135° respectively, i.e. in directions where the mode under consideration halves the angle between the *xy* principal directions. The shape and envelope of the stability boundaries are a strong function of the engagement conditions and position-varying strengths of directional modes. An ideal machine design must have circular stability boundary, i.e. identical depth of cut limits in all directions, which is only possible if the structural dynamics of the machine are uniform in all feed directions.

Minimum limits of ~5.4 mm at the 142° and 322° feed orientations are observed when the tool is at the bottom position; and, ~3 mm at the 52° and 232° feed orientations for when the tool is at the mid position. The absolute minimum limit occurs however when the tool is at the top position of the Z stroke; being ~1.8 mm at the 52° and 232° feed orientations. This is mainly due to the fact that the dynamic stiffness of modes in the *X* and *Y* directions is similar in magnitude and is a minimum at this position (see Fig. 3). The feed-directional chatter spectrum in Fig. 8(b) also shows that chatter occurs at ~41–42 Hz, which is close to the two column bending modes in the XZ and YZ planes, when the tool is at the top position. The dynamic stiffness of the *Y* directional column mode is sufficiently higher than the *X* directional mode when the tool is at the mid and bottom positions—hence the chatter frequency spectrum is dominated by the column bending mode in the XZ plane. Having identified the column mode(s) as the cause of limited productivity due to chatter, they need to be stiffened.

5. Structural design modifications and topology optimization

In order to achieve the target productivity goal, the dynamic stiffness of the modes limiting productivity is increased through structural modification. The dominant modes being the bending and torsion of the column (see Figs. 3 and 4), the column substructure is stiffened through addition of flange stiffeners and internal cross ribs. These modifications shown in Fig. 9 result in increase in mass of the column by ~15%, which is contrary to the objective of development of light-weight machine tools. Hence, a subsequent topology optimization is carried out on the Hypermesh® platform [26] to optimize material distribution within the column design space while minimizing its volume.

The design space for the column is defined as all the space other than the contacting interfaces. A new design concept is found by subjecting the TCP to loads representing machining forces of $F_x=F_y=F_z=3000$ N while respecting constraints on compliance. Optimization investigations have been conducted at

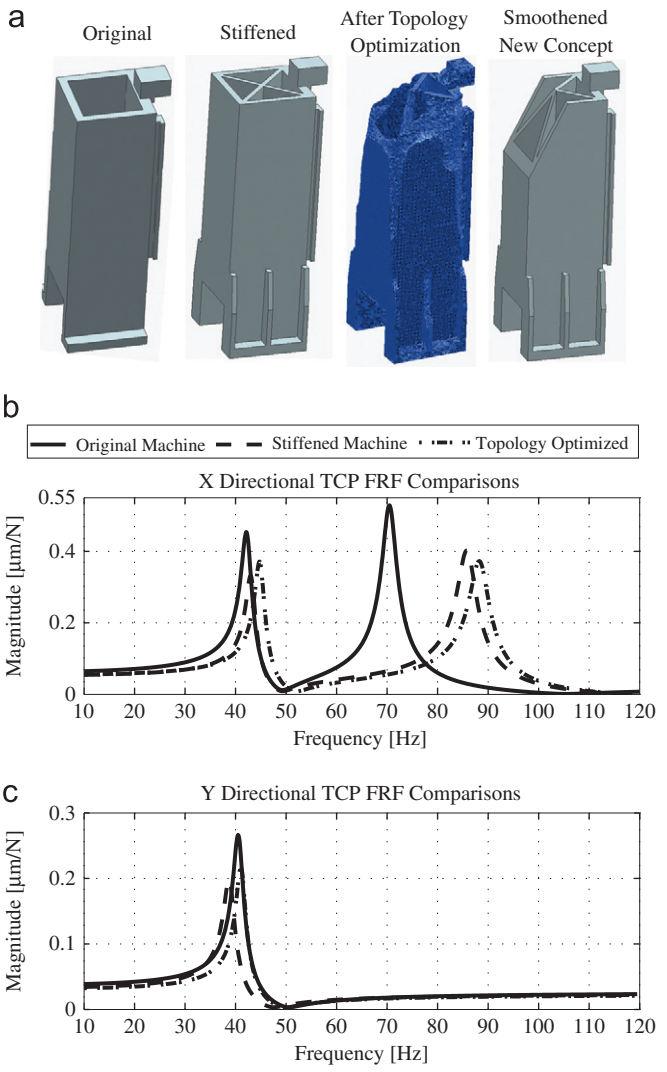

Fig. 9. Comparison of: (a) Original, modified, optimized, and smoothened column models; (b) the corresponding *X* direction TCP FRFs; and (c) *Y* direction TCP FRFs for original and the modified machine models.

all three positions of the spindle housing described earlier, and the final design concept is shown in Fig. 9(a). The new design concept for the column has the same mass as that of the original column model, i.e. a ~15% reduction in mass from the stiffened model was achieved through optimization. This design concept is smoothened into a suitable geometry-based CAD model for further analysis.

The procedure given in the flowchart in Fig. 1 is followed again with the new column concept to obtain the new synthesized reduced machine tool model. The reduced model's dynamic response at the TCP for the original, stiffened and subsequently optimized machine model is compared in Fig. 9(b, c) for a representative condition when the tool is at the top position. For comparisons, a uniform damping ratio of $\zeta = 0.02$ has been assumed.

An increase in dynamic stiffness by ~20% for each of the first bending modes in the XZ and YZ planes; and by ~30% for the mode at ~90 Hz is evident from TCP FRF comparisons in Fig. 9(b, c), in which comparisons are limited to 120 Hz, i.e. the frequency range affected by the structural modifications. The increase in the natural frequencies of the low-frequency modes is due to stiffening. The dynamic response with the optimized topology is equivalent to the response with the stiffened structure with the advantage of having less overall structural mass. The static stiffness for the modified machine design now ranges from 20–22 N/μm (depending on tool position), an increase of ~40% over the previous range of 14–16 N/μm. The dynamic response for the modified optimized new machine concept at all positions was updated using measured modal damping values as was carried out in Section 3.

Stability was simulated with the same tool and cutting conditions as before, but with the modified machine response; and the stability results are compared with the values of the original machine model for the three positions as before, see Fig. 10.

As is evident from Fig. 10, the new absolute stability limit at the top position is ~2.5 mm at the 52° and 232° feed-orientations, an increase of ~35% over the limit achievable with the original machine model. At the mid position, the new absolute limit is ~3.6 mm, an improvement by ~20% over the earlier ~3 mm limit; and at the bottom position, the new absolute limit is ~8 mm, an increase of ~45% over the earlier ~5.6 mm limit, and well above the target level of 4 mm for all feed directions. The shape and envelope of the stability boundaries are different than the original design due to the change in position-varying directional compliances for the modified structure. Structural modifications result in an increase in the stability envelope leading to higher absolute stability limit for a wider range of feed directions, even exceeding the target productivity levels of 4 mm at certain feed directions for when the tool is at the top and mid positions respectively; which is a significant improvement over the earlier design. Further improvements, if necessary, to meet the target 4 mm depth of cut at all working positions are possible by modifying (stiffening) other substructures, or, by integrating active/ passive damping mechanisms—all of which are facilitated by the rapid iterative procedure presented in this paper.

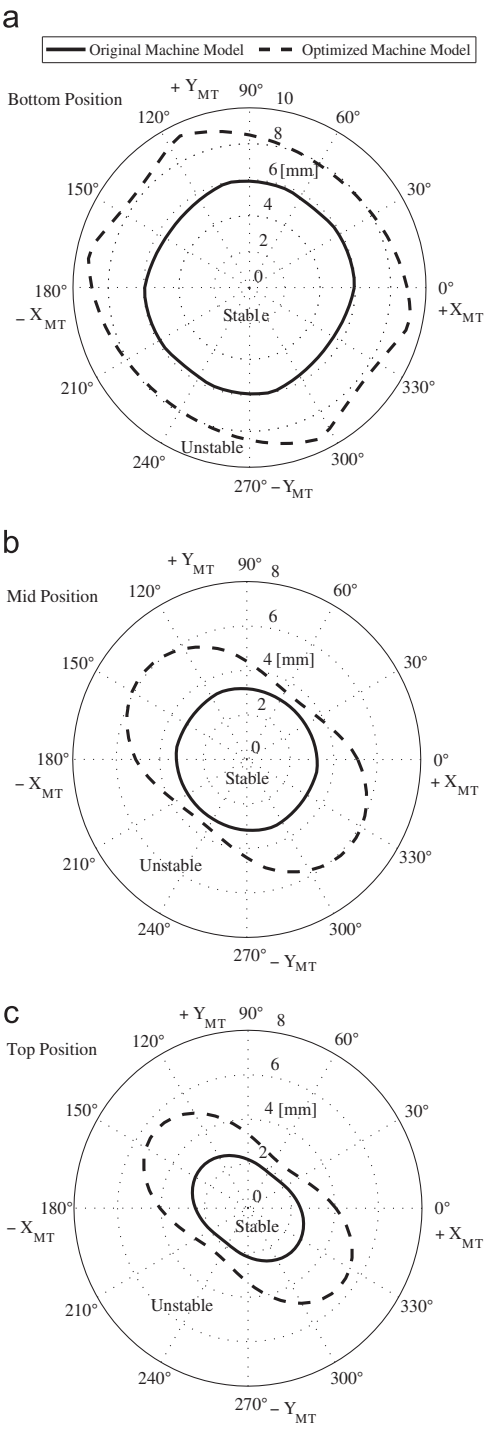

Fig. 10. Feed-directional stability comparison for original and modified (optimized) machine model at two different tool positions: (a) bottom; (b) mid; and (c) top.

6. Conclusions

This paper demonstrates the feasibility of a virtual engineering approach for designing machine tools to improve their dynamic stiffness hence achieving targeted productivity by considering the position-dependent process–machine interactions. A position-dependent, substructurally synthesized reduced order machine model is presented which efficiently simulates dynamic response. The model facilitates rapid investigation of design alternatives without having to use the presently used time consuming full FE models. The model is also validated against measurements.

For a defined set of representative milling operations and target productivity levels for which the machine is being envisaged, the effects of position and feed-direction-dependent compliances and machining stability are investigated. It is shown that the proposed reduced order substructural model allows rapid redesign and analysis of components which limit the productivity due to low compliance. Though the design methodology was applied to a specific kinematic configuration and for a given set of

machining operations, the methodology proposed is generic and may be extended to virtual evaluation of any machine tool. The proposed virtual machine concept facilitates total system simulation, including the dynamics of the control and mechanical parts of the machine; making it possible to assess design suggestions and to perform system optimization at an early stage of development.

Acknowledgments

This research has been supported by the NSERC CANRIMT Research Grant. The authors would also like to acknowledge Dr. Tzuo-Liang Lo from ITRI, Taiwan, for his technical assistance with topology optimization.

References

[1] Y. Altintas, C. Brecher, M. Weck, S. Witt, Virtual machine tool, Annals of CIRP 54 (2005) 115–138.
[2] M.F. Zaeh, T. Oertli, J. Milberg, Finite element modelling of ball screw feed drive systems, Annals of CIRP 53 (2004) 289–292.
[3] Y. Cao, Y. Altintas, A general method for the modeling of spindle-bearing systems, ASME Journal of Mechanical Design 126 (2004) 1089–1104.
[4] P. Kolar, M. Sulitka, M. Janota, Simulation of dynamic properties of a spindle and tool coupled with a machine tool frame, International Journal of Advanced Manufacturing Technology 54 (2011) 11–20.
[5] M. Mori, Z. Piner, K. Ding, A. Hansel, Virtual evaluation for machine tool design, in: Proceedings of the 9th Biennial ASME Conference on Engineering Systems Design and Analysis, Haifa, Israel, 2008.
[6] J.J. Zulaika, F.J. Campa, L.N. Lopez de Lacalle, An integrated process—machine approach for designing productive and lightweight milling machines, International Journal of Machine Tools and Manufacture 51 (2011) 591–604.
[7] J.-P. Hung, Y.-L. Lai, C.-Y. Lin, T.-L. Lo, Modeling the machining stability of a vertical milling machine under the influence of the preloaded linear guide, International Journal of Machine Tools and Manufacture 51 (2011) 731–739.
[8] G. Bianchi, F. Paolucci, P. Van den Braembussche, H. Van Brussel, F. Jovane, Towards virtual engineering in machine tool design, Annals of CIRP 45 (1996) 381–384.
[9] M. Zatarain, E. Lejardi, F. Egana, Modular synthesis of machine tools, Annals of CIRP 47 (1998) 333–336.
[10] G. Reinhart, M. Weißenberger, Multibody simulation of machine tools as mechatronic systems for optimization of motion dynamics in the design process, in: Proceedings of the IEEE/ASME International Conference on Advanced Intelligent Mechatronics, Atlanta, USA, 1999, pp. 605–610.
[11] M.F. Zaeh, D. Siedl, A. New, Method for simulation of machining performance by integrating finite element and multi-body simulation for machine tools, Annals of CIRP 56 (2007) 383–386.
[12] J. Fleischer, C. Munzinger, M. Trondle, Simulation and optimization of complete mechanical behaviour of machine tools, Production Engineering Research and Development 2 (2008) 85–90.
[13] M.M. da Silva, O. Bruls, J. Swevers, W. Desmet, H. Van Brussel, Computer-aided integrated design for machines with varying dynamics, Mechanism and Machine Theory 44 (2009) 1733–1745.
[14] A. Jonsson, J. Wall, G. Broman, A virtual machine concept for real-time simulation of machine tool dynamics, International Journal of Machine Tools and Manufacture 45 (2005) 795–801.
[15] P. Sekler, M. Voss, A. Verl, Model-based calculation of the system behavior of machine structures on the control device for vibration avoidance, International Journal of Advanced Manufacturing Technology 58 (2012) 1087–1095.
[16] M. Law, A.S. Phani, Y. Altintas, Position-dependent multibody dynamic modeling of machine tools based on improved reduced models, ASME Journal of Manufacturing Science and Engineering, http://dx.doi.org/10.1115/1.4023453, in press.
[17] T.L. Schmitz, R. Donaldson, Predicting high speed machining dynamics by substructure analysis, Annals of CIRP 49 (2000) 303–308.
[18] G. Heirman, W. Desmet, Interface reduction of flexible bodies for efficient modeling of body flexibility in multibody dynamics, Multibody System Dynamics 24 (2010) 219–234.
[19] R.D. Cook, D.S. Malkus, M.E. Plesha, R.J. Witt, Concepts and Applications of Finite Element Analysis, fourth ed., John Wiley and Sons, Inc., NJ, USA, 2001.
[20] T.L. Schmitz, K.S. Smith, Machining Dynamics—Frequency Response to Improved Productivity, Springer, NJ, USA, 2009.
[21] ANSYS V12, Documentation for ANSYS, 2009.
[22] CUTPRO V9.3, Advanced Machining Simulation Software. (〈www.malinc.com〉).
[23] THK Global. (〈www.thk.com〉).
[24] Y. Altintas, E. Budak, Analytical prediction of stability lobes in milling, Annals of CIRP 44 (1995) 357–362.
[25] Z.M. Kilic, Y. Altintas, Effect of unmatched spindle dynamics on the material removal rates in milling operations, in: Proceedings of MTTRF 2011 Meeting, Chicago, Illinois, USA, 2011, pp. 19–24.
[26] HyperMesh V11, Altair HyperWorks.